Nanoscale

PAPER

Check for updates

Hybrid multimodal contrast agent for multiscale *in vivo* investigation of neuroinflammation†

Szilvia Karpati,[a] Violaine Hubert,[b] Inès Hristovska,[c] Frédéric Lerouge,*[a] Frédéric Chaput,[a] Yann Bretonnière, [ID][a] Chantal Andraud,[a] Akos Banyasz,[a] Guillaume Micouin,[a] Maëlle Monteil,[d] Marc Lecouvey,[d] Marion Mercey-Ressejac,[e] Arindam K. Dey, [ID][e] Patrice N. Marche,[e] Mikael Lindgren,[f] Olivier Pascual,[c] Marlène Wiart[b] and Stephane Parola [ID]*[a]

Neuroinflammation is a process common to several brain pathologies. Despite its medical relevance, it still remains poorly understood; there is therefore a need to develop new *in vivo* preclinical imaging strategies to monitor inflammatory processes longitudinally. We here present the development of a hybrid imaging nanoprobe named **NP3**, that was specifically designed to get internalized by phagocytic cells and imaged *in vivo* with MRI and bi-photon microscopy. **NP3** is composed of a 16 nm core of gadolinium fluoride (GdF_3), coated with bisphosphonate polyethylene glycol (PEG) and functionalized with a Lemke-type fluorophore. It has a hydrodynamic diameter of 28 $\pm$ 8 nm and a zeta potential of -42 ± 6 mV. The MR relaxivity ratio at 7 T is $r_1/r_2 = 20$; therefore, **NP3** is well suited as a $T_2/T_2{}^*$ contrast agent. *In vitro* cytotoxicity assessments performed on four human cell lines revealed no toxic effects of **NP3**. In addition, **NP3** is internalized by macrophages *in vitro* without inducing inflammation or cytotoxicity. *In vivo*, uptake of **NP3** has been observed in the spleen and the liver. **NP3** has a prolonged vascular remanence, which is an advantage for macrophage uptake *in vivo*. The proof-of-concept that **NP3** may be used as a contrast agent targeting phagocytic cells is provided in an animal model of ischemic stroke in transgenic CX3CR1-GFP/+ mice using three complementary imaging modalities: MRI, intravital two-photon microscopy and phase contrast imaging with synchrotron X-rays. In summary, **NP3** is a promising preclinical tool for the multiscale and multimodal investigation of neuroinflammation.

Introduction

Stroke is one of the leading causes of mortality worldwide accounting for 11.8% of global deaths.[1] Ischemic stroke is induced by transient or permanent occlusion of a cerebral artery.[2] The perturbation of blood flow leads to neuronal death

in the most severely hypoperfused areas. In addition, a complex sequence of inflammatory events occurs following ischemic stroke, among which is the activation of infiltrating and brain resident macrophages (microglia).[3] This neuroinflammatory response may lead to secondary brain damage and thus represents a potential therapeutic target. However, the complex role of neuroinflammation is not well understood to date. There is thus a need to develop new *in vivo* preclinical imaging strategies to follow inflammatory processes longitudinally at the acute stage of ischemic stroke, in order to better understand the physiopathology, as well as to monitor the effects of anti-inflammatory treatments prior to their clinical translation.

Today, PET imaging of microglia activation using 18 kDa translocator protein (TSPO) tracers is at the forefront for translational *in vivo* molecular imaging of neuroinflammation following stroke.[4] One limitation of this approach, however, is that at the acute stage of ischemic stroke (<72 h), the number of activated microglia is below the limit of detection.[4] Therefore, currently PET imaging cannot be used to monitor neuroinflammation in this crucial time-window, where immunomodulatory treatments may be the most effective. The non-

[a]*Université de Lyon, Ecole Normale Supérieure de Lyon, CNRS UMR 5182, Université Lyon 1, Laboratoire de Chimie, 46 allée d'Italie, F69364 Lyon, France. E-mail: stephane.parola@ens-lyon.fr, frederic.lerouge@ens-lyon.fr*
[b]*Univ-Lyon, CarMeN laboratory, Inserm U1060, INRA U1397, INSA Lyon, Université Claude Bernard Lyon 1, F-69600 Oullins, France*
[c]*Institut NeuroMyoGène, Université Claude Bernard Lyon 1, CNRS UMR 5310, INSERM U1217, Université Lyon, Villeurbanne 69100, France*
[d]*Université Sorbonne Paris Nord, Laboratoire CSPBAT, CNRS UMR 7244, F-93017 Bobigny Cedex, France*
[e]*Institute for Advanced Biosciences, Université Grenoble-Alpes, INSERM U1209, CNRS UMR5309, La Tronche, France*
[f]*Norwegian University of Science and Technology – Department of Physics, Høgskoleringen 5, Realfagbygget, 7491 Trondheim, Norway*
†Electronic supplementary information (ESI) available. See DOI: 10.1039/d0nr07026b

invasive nature of MRI and CT, in conjunction with their wide availability, make them particularly suitable for longitudinal neurologic imaging studies. Magnetic resonance imaging (MRI) or computed tomography (CT) coupled with the administration of metallic nanoparticles (such as iron oxides) represents an attractive tool for studying inflammation.[5,6] After their intravenous injection, the nanoparticles get internalized by activated phagocytic cells, mostly macrophages. Since phagocytic cells strongly participate in the development of inflammation processes, these imaging approaches are used as a surrogate marker of inflammatory processes. The advantage of using metal-based nanoparticles for this purpose is the possibility to combine complementary imaging modalities at different scales to track the labelled macrophages. One of the limitations of these techniques, however, is the fact that the signals seen on postcontrast images may have different origins than nanoparticle-labelled cells, for instance microhemorrhages or microcalcifications. One way to address this issue is to design contrast agents that may be imaged with element-specific imaging tools, for instance fluorine for MRI[7] and gadolinium for spectral photon counting CT.[8] In addition, to further validate the biological substrate of MR and CT signals, there is a need to complement these techniques with imaging tools that are better resolved spatially and provide information about specific immune cells. Intravital two-photon induced fluorescence imaging is a good candidate due to its high sensitivity, resolution at sub-cellular scale, the possibility of real-time monitoring and the availability of transgenic mice such as CX3CR1-GFP/+ mice that have green fluorescent microglia and macrophages.[9]

Consequently, the aim of our study was to design a multi-modal contrast agent adapted simultaneously for three imaging modalities (MRI, CT and two-photon microscopy) and optimized for the passive targeting of phagocytic cells. In addition, because our primary application is ischemic stroke, we added the specification that our imaging probe should be able to cross the blood brain barrier (BBB) following focal cerebral ischemia. Nanoparticles are well-suited for this aim because they circulate longer than small molecular weight contrast agent and hence can accumulate in inflammatory regions with high phagocytic activity. Because gadolinium is particularly well-suited for both MRI and spectral photon counting CT,[10] we here propose to use functionalized gadolinium fluoride (GdF$_3$) nanoparticles as a contrast platform.

Due to its very low solubility (less than 3×10^{-5} mol L^{-1}) in aqueous media,[11] GdF$_3$ is considered as one of the most stable gadolinium compounds. Moreover, nanostructured materials concentrate a high amount of gadolinium ions, giving rise to high contrast-to-noise ratio both in MRI and CT. Recently, we demonstrated that GdF$_3$ nanoparticles were optimal for *in vivo* angiography with spectral photon counting CT, due to their efficient X-ray attenuation properties and long vascular remanence.[12]

In the present work, size and coating of the GdF$_3$ platform were finely tuned to allow the passive targeting of phagocytic cells. The probe was further functionalized with a dedicated two-photon microscopy fluorophore. This paper reports the synthesis and characterization of this novel imaging nanoprobe. We verified that the nanoprobe was internalized *in vitro* by bone-marrow derived macrophages. We provide data on cytotoxicity as well as *in vivo* biodistribution and pharmacokinetic. Finally, the proof-of-concept of its potential for multi-scale and multimodal imaging of neuroinflammation was obtained in a murine model of ischemic stroke using three complementary imaging modalities: MRI, intravital two-photon microscopy and phase contrast imaging with synchrotron X-rays.

Experimental

Synthesis of NP1

4.83 g (0.013 mol) of GdCl$_3$·6H$_2$O (Alfa Aesar 99.9%) was stirred at room temperature in 2 mL of ethylene glycol (EG) until complete dissolution and was further diluted with 3 mL of 2-pyrrolidinone. This solution was added to a solution of 1.1 mL (0.0316 mol) 50% hydrofluoric acid in 24 mL of 2-pyrrolidinone. The mixture was then heated up to 170 °C for 1.5 h in a 50 mL stainless steel Teflon lined digestion pressure vessel. The obtained suspension was cooled down to room temperature and the particles were precipitated in acetone. The colloidal nanoparticles were purified by several centrifugation-redispersion cycles using methanol as washing solvent. After purification, the nanoparticles were suspended in water and freeze-dried for further use.

Synthesis of NP2 and NP3

First step: 600 mg of GdF$_3$ NP were suspended in 2 mL of ultra-pure water. To this suspension was added a solution of a mixture of two types of bifunctional bisphosphonate-terminated PEGs in water: 40.3 mg (4.67×10^{-5} mol; 5 mol% of total ligand quantity) of **2** and 899 mg (8.87×10^{-4} mol) of **1** in 2 mL of ultrapure water. The homogeneous suspension was magnetically stirred at 80 °C for 2 h and stirred at room temperature for one night. The as prepared functionalized nanoparticles **NP2** were subjected to dialysis for one week to remove excess ligand and then were freeze-dried. In a second step a suspension of **NP2** (452 mg in 1.5 mL of water) was added to a solution of **3** (5.5 mg) in ethylene glycol (6.5 mL). The mixture was heated to 150 °C and stirred for 5 h. The obtained fluorescent and coated NPs (**NP3**) were first precipitated in acetone, washed with ethanol, and centrifuged several times, until the supernatant becomes colorless.

Analysis of particle morphology and composition

DLS and zeta potential measurements were performed on aqueous suspensions of the particles, by a Malvern Instruments Nano ZS. XPS analysis was carried out by PHI Quantera SXM instrument, with monochromatic Al Kα source. TEM images were acquired using a JEOL JEM 1400 equipped with a Gatan Orius 600 camera and operated at 120 kV. XPS measurements were carried out with a PHI Quantera SXM

photoelectron spectrometer using Al Kα radiation ($h\nu$ 1486.7 eV). MultiPak software was used for the fitting procedure.

Two-photon absorption spectroscopic study

For two-photon spectroscopic study the excitation source was a tunable femtosecond Ti-sapphire laser (Chameleon Ultra I, Coherent) producing 140 fs pulses. The excitation beam was focused by a 100 mm focal length lens into a 10×10 mm spectroscopic quartz (QZS) cell containing the sample. The emitted fluorescence was collected at right angle and delivered to a spectrometer (AvaSpec-EVO, Avantes) *via* an optical fiber. The cell position was adjusted so that the optical path was minimized in the cell on both the excitation and the detection side; this allowed reducing artefacts due to inner-filter effects and scattering. Additionally, low-pass filters were used between the cell and the entrance of the fiber to prevent the scattered laser light from entering the spectrometer as much as possible. Here fluorescein in a pH 13 aqueous solution was used as the two-photon reference standard.[13]

Cytotoxicity assays

Cell lines: **NP3** nanoparticle potential cytotoxicity was assessed on four human cell lines, all supplied by the American Type Culture Collection (ATCC). A549, epithelial-like cells from human lung, were cultivated in DMEM 4.5 g L^{-1} glucose + GlutaMAX medium supplemented with 10% fetal calf serum (FCS) and 1% penicillin–streptomycin. THP-1, monocytes from human peripheral blood, were cultivated in RPMI 1640 + GlutaMAX medium supplemented with 10% FCS, 1% penicillin–streptomycin, 1% pyruvate and 4.5 g L^{-1} glucose. HepG2, human hepatocytes, were cultivated in MEM + GlutaMAX medium supplemented with 10% FCS, 1% penicillin–streptomycin and 1% pyruvate. Finally, HEK 293T, embryonic kidney cells from human, were cultivated in the same medium than HepG2 cells. *Cell survival assays*: **NP3** impact on cell lines was evaluated using two complementary assays: the LDH (lactate dehydrogenase) assay, assessing cell membrane damages and the MTT (3-(4,5-dimethylthiazol-2-yl)-2,5-diphenyltetrazolium bromide) assay, assessing mitochondrial activity. Briefly, the different cell lines were seeded in 96-well plates at 10^5 cells per mL for A549, HEK and HepG2, and 5×10^5 cells per mL for THP-1, and incubated for 24 h at 37 °C and 5% CO_2. After 24 h, cells were exposed to different **NP3** concentrations (0.5 nM to 5000 nM). Cell survival assays have been performed at 48 hours and 72 hours after **NP3** incubation. For LDH assay, cells were incubated with 100 μL of CytoToxOne reagent for 10 minutes at 22 °C. 50 μL of stop solution were then added in each well and cell death is measured by fluorescence with ELISA plate reader (Victor, PerkinElmer) at λex = 544 nm and λem = 572 nm. For MTT assay, 10 μL of MTT Sigma-Aldrich solution (5 mg mL^{-1} in PBS) were added to each well, and the 96-well plates were incubated for 2 hours at 37 °C. 100 μL of lysis buffer (SDS 10%) were then added to each well, and after 3 hours of agitation, cell viability was determined by absorption measurement (λ = 570 nm) with ELISA plate reader (Victor, PerkinElmer).

Animal model and *in vivo* experimental timeline

All procedures involving animals and their care were carried out according to the European regulation for animal use (EEC council directive 2010/63/UE, OJ L 276, Oct. 20, 2010). This study was approved by our local ethic committee "Comité d'éthique pour l'Expérimentation Animale Neurosciences Lyon" (CELYNE – CNREEA number: C2EA – 42).

At D0, transgenic CX3CR1-GFP/+ mice expressing green fluorescent protein (eGFP) in microglia/macrophages were subjected to a model of ischemic stroke (males, $n = 4$). Permanent occlusion of the distal middle cerebral artery (pMCAo) was induced in the anesthetized (isoflurane, 2%, ISO-VET, Piramal Healthcare, Morpeth, UK) animals, using the application of iron chloride (10% $FeCl_3$) solution, according to the procedure described previously by Karatas *et al.*[14] One mouse not submitted to pMCAo served as control. One day after the occlusion (D1), all the mice ($n = 5$) underwent a basal MRI session to assess the presence of an ischemic lesion. Immediately after, the mice were injected into the tail vein with 2 mmol kg^{-1} of **NP3** ($n = 5$). Following the injection, a subgroup of mice (pMCAo mouse, $n = 2$; control mouse; $n = 1$) was submitted to a second surgical intervention for intravital two-photon microscopy imaging: after the skull was thoroughly thinned, a 6 mm diameter polyamide (MRI-compatible) implant was placed over an area encompassing both the ischemic lesion and some extralesional tissue. On the same day (D1), these mice underwent a 2 hours-two-photon excitation microscopy (TPEM) imaging session. In order to have pre-**NP3** and post-**NP3** TPEM images, the control mouse was intravenously injected with **NP3** during the TPEM session and was also imaged 24 hours after **NP3** injection (D2). To assess the potential of TPEM for **NP3** longitudinal follow-up, one of the pMCAo mice was submitted to a second TPEM imaging session. Finally, all mice ($n = 5$) underwent a post-**NP3** MRI session 48 hours following **NP3** injection (D3) and were then euthanized. *Ex vivo* X-ray phase contrast imaging was performed on the brain of pMCAo mouse.

In vitro and *in vivo* MRI

All the MRI exams were performed on a 7 T horizontal-bore Bruker Advance II rodent imaging system (Bruker Biospin, Ettlingen, Germany). For the *in vivo* MR imaging exams, mouse anaesthesia was induced with a mixture of air and 3.5% isoflurane and maintained with 2% isoflurane. The animals were placed in an MRI-compatible mouse cradle, and the body temperature was monitored thanks to circulating heated water. *Relaxivity measurements*: To quantify the r_1 and r_2 relaxivities of **NP3** (in mM^{-1} s^{-1}), phantoms have been prepared with a range of twelve gadolinium concentrations going from 0 to 5 mM in saline. To reach the appropriate concentrations, **NP3** phantoms were prepared using a 0.5 M stock solution dissolved in saline. Measurements were then performed at 25 °C. T_1 maps were obtained from a fast imaging with steady-state procession (FISP) sequence (TE/TR = 2.1/4.2 ms; inversion time (TI): 73.8 ms; 32 echoes) by fitting an inversion/recuperation function to the data. T_2 maps were

obtained from a multiple spin-echo sequence (MSME; TE [interecho delay]/TR = 50/5000 ms; 24 echoes) by fitting a monoexponential function to the data. *Biodistribution and pharmacokinetic*: To evaluate **NP3** biodistribution and pharmacokinetic, C57Bl/6 mice (males, n = 4) were imaged using a 35 mm inner diameter whole-body transmit-receive coil for signal acquisition. To avoid movement artifacts due to the breathing, the acquired sequence was triggered on mouse respiratory rhythms. Abdominal axial T_1 images were obtained with a dynamic RARE 2D sequence (TE/TR = 7.51/960.77 ms; FA = 90; number of averages = 2; acquisition time 1.32 min; number of repetitions = 25). 37 slices were acquired from the top of the heart to the bottom of the liver, using a FOV of 35 × 35 mm^2, a slice thickness of 1 mm and a matrix of 128 × 128. **NP3** (2.0 mmol kg^{-1}) was injected as a bolus *in vivo* in the magnet between the second and the third repetitions. MR signal changes in time were analyzed in regions of interest (ROI) and normalized using pre-contrast values. *Imaging of stroke-induced animals*: A 50 mm inner diameter birdcage coil was used for transmission and a 15 mm diameter surface coil was used for reception. The following axial sequences were used: a spin-echo T_2-weighted image (T_2-WI), TE/TR = 43.8/5000 ms, bandwidth = 40 kHz, number of averages = 6, acquisition time 12 min; a T_2-star gradient-echo (GRE) FLASH sequence (T_2*-WI), TE/TR = 6/750 ms, bandwidth = 40 kHz, flip angle (FA) = 20°, number of averages = 8, acquisition time 19 min. For each sequence, 25 slices were acquired from the olfactory bulb to the cerebellum of the mice, using a field of view (FOV) of 20 × 20 mm^2, a slice thickness of 500 μm and a matrix size of 256 × 256.

Two-photon excitation microscopy (TPEM)

For the *in vivo* TPEM imaging sessions, mice have been anesthetized with a mixture of ketamine (100 mg kg^{-1}) and medetomidine (1 mg kg^{-1}). Their body temperature was maintained at 37 °C using a heating pad. TPEM observations were performed on a Bruker Ultima microscope (Insight 3X laser, Spectra Physics), equipped with a 20× water-immersion objective (0.95 N.A. Olympus). Green (CX3CR1-GFP/+ cells) and red (**NP3** particles) fluorescence were separated by a 560 nm dichroic mirror coupled to 525/50 nm and 650/40 emission filters.

30–45 consecutive *Z*-stacks were acquired at a depth of 50–150 μm, with a step size of 1 μm and a resolution of 521 × 521 pixels. ImageJ and Icy (open source software created by BioImage Analysis Lab, Institut Pasteur, France; http://icy.bioimageanalysis.org/) were used for image treatment, and drift correction was applied with a custom-written Matlab software (used for image correction for drift during the acquisition).

X-ray phase contrast tomography

For *ex vivo* phase contrast tomography, mice have been euthanized by intracardiac perfusion with 4% PFA. Brains were then extracted and dehydrated in successive ethanol baths. In-line phase contrast tomography was performed on beamline ID17 of the European Synchrotron Radiation Facility (ESRF) in Grenoble at 26 keV. An indirect detection-based detector with a LuAg scintillator, standard microscope optics and a 2048 ×

2048 pixel CCD camera was positioned 3 m from the sample to obtain phase contrast. The whole-brain data set was acquired at an isotropic pixel size of 7.5 μm. Acquisition time of the 3000 projections was <5 minutes per brain. Reconstruction was performed with Paganin algorithm by setting γ/β to 1000 as in.[15]

Results and discussion

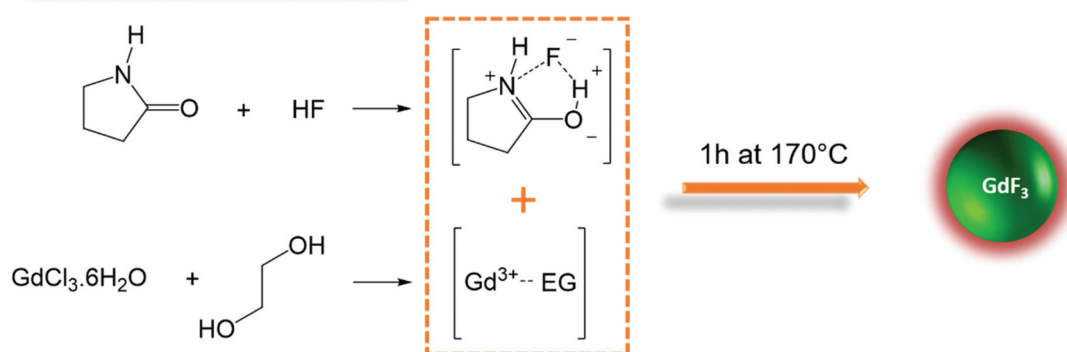### Nanoparticle core synthesis (NP1)

The synthesis of the GdF$_3$ inorganic core (**NP1**) was adapted from a previously described method[12] under solvothermal conditions in a mixture of ethylene glycol (EG) and 2-pyrrolidinone.[16–18] The originality of this method consists in the generation of various complexes involving F$^-$ and Gd^{3+} ions (Scheme 1A) leading to an improved control of nanoparticle morphology and size distribution. As shown by transmission electron microscopy (TEM) observations (Fig. S1A†), **NP1** are spheroidal and slightly elongated. Their hydrodynamic diameter determined by dynamic light scattering (DLS) measurements (Fig. S1B†) is 16 ± 5 nm, with low polydispersity (polydispersity index, PDI: 0.16). The X-ray powder diffraction (XRPD) pattern (Fig. S1C†) shows high crystallinity of **NP1** and comparison of the peaks to the reference pattern ICSD card 00-012-0788 demonstrates the pure orthorhombic phase (*Pnma* space group) of GdF$_3$. The positive zeta potential +45 ± 10 mV measured for **NP1** in water, suggests an excess of Gd^{3+} ions on the surface, which is in accordance with the observed 67.7 atomic% of gadolinium, determined by X-ray photoelectron spectroscopy (XPS) analysis (Table S1†). Furthermore, this elemental composition analysis reveals a F/Gd atomic ratio of 0.39 at the surface. Such small ratio (expected F/Gd ratio is 3) is explained by two aspects. First, the surface composition of a nanoparticle is always different from the bulk composition (surface effects, crystal defects *etc.*) and segregation of elements is frequently observed.[19] XPS is a surface scanning technique, with a penetration depth of a few nanometers. In our case it was approximately 3 nm, therefore the observed composition was not the composition of bulk GdF$_3$. The second reason is that in our synthesis conditions F/Gd is kept lower than the stoichiometric ratio, because F$^-$ excess induces in the case of gadolinium a mixture of two crystalline phases: orthorhombic and hexagonal. However, as it was mentioned before, according to X-ray powder crystallographic measurements, the overall crystalline phase corresponds effectively to the orthorhombic GdF$_3$ phase (Fig. S1C†). According to attenuated total reflection Fourier-transform infrared spectroscopy (ATR-FTIR) measurements, small organic capping molecules identified as the open form of solvent molecule 2-pyrrolidinone, are present on the surface (Fig. S2A†).
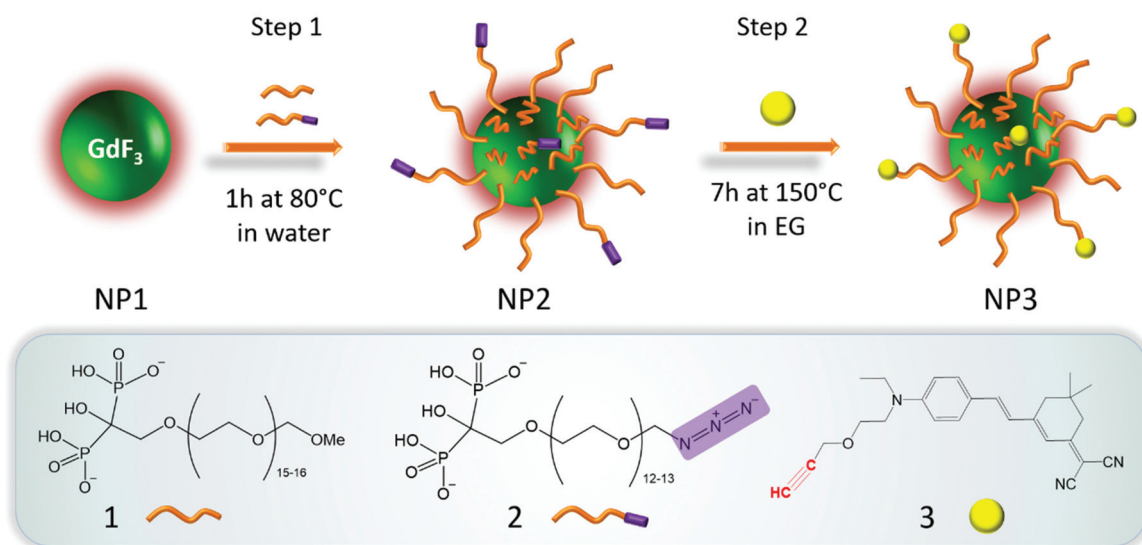
Core–shell nanoparticles (NP2)

The surface modifications of **NP1** was achieved following a two-step approach presented in Scheme 1B. The first step consists in the preparation of functional particles **NP2**, through the grafting of a mixture of two bisphosphonate PEG deriva-

Scheme 1 A) Solvothermal synthesis of GdF$_3$ nanoparticles (**NP1**). The solvent, 2-pyrrolidinone is complexing the fluoride ion (source of fluoride is HF) and ethylene glycol chelates gadolinium(III) ions (from GdCl$_3$). The mixture is heated to 170 °C for 1 h in a Teflon lined autoclave to give **NP1** nanoparticles. (B) The surface of **NP1** is modified in two steps: first, PEG-ligands, **1** and **2** are grafted and chromophore **3** is coupled in a second step.

tives with and without azide reactive groups (compounds **1** and **2**, respectively). The synthesis of these ligands developed by Lecouvey *et al.* has been described in detail elsewhere.[20] The bisphosphonate functions allow strong anchoring *via* multidentate chelation of gadolinium ions.[21,22] While ligand **1** is used to ensure biocompatibility, **2** allows coupling with the fluorophore **3** through its −N$_3$ group. The molar percentages of ligand **1** and ligand **2** were set at respectively 95% and 5%. This ratio was optimized taking into consideration the stability of the particle in biological media and the optical properties for appropriate two-photon fluorescence imaging. The second step focuses on the coupling of fluorophore **3** (the synthesis of **3** is described in ref. 23) with the azide functions on the PEG-coated nanoparticle **NP2**.

The success of multifunctional PEG grafting was first evaluated by ATR-FTIR spectroscopy. Infrared spectrum of **NP2**

(Fig. 1A) as compared to **NP1** (Fig. S2A,† red spectrum) shows typical signatures of PEG species, with bands at 2869 cm^{-1} and around 1100 cm^{-1} for ether C–H and C–O–C stretching modes respectively.[24] The presence of the organic layer around the particles was also evidenced by DLS (Fig. 1B) where hydrodynamic diameter increases from 16 ± 5 nm (blue signal) to 21 ± 7 nm (red signal). Charge surface of the particles was evaluated with zeta potential measurements, showing a switch from a positive (+45 ± 10 mV) to a negative value (−28 ± 3 mV) due to the deprotonated bisphosphonate moieties linked to surface gadolinium atoms. Grafting of PEG-ligands **1** and **2** on the particle was also evidenced by thermogravimetric analysis (TGA) (Fig. S2B†) where a significantly higher weight loss (29.3%) corresponding to organics was observed in the case of **NP2** compared to **NP1**.
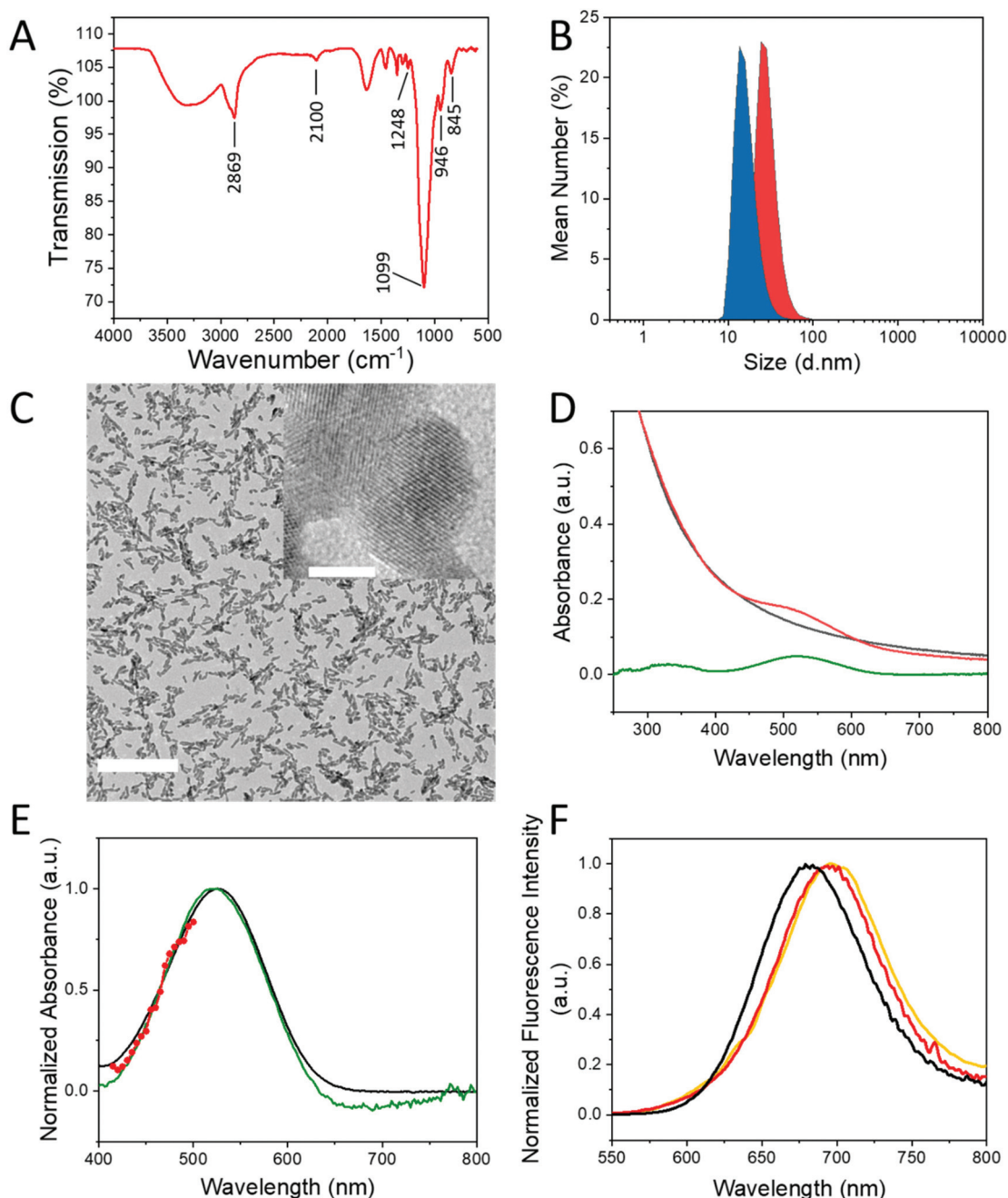
Fig. 1 (A) FTIR-ATR spectra of **NP2** nanoparticles. (B) DLS measurements of the particles before (**NP1**) any surface modification (blue) and after PEGylation and fluorophore grafting (**NP2**) (red). (C) TEM image of the particles after surface modification (**NP3**). Scale bar is 50 nm for larger image and 5 nm for the inset. (D) Absorption spectra of **NP3** (red line) and **NP2** (black line) are compared. The difference of these two spectra (green line) reveals the absorbance of the chromophore without the scattering due to the particles. (E) Differential absorbance (green) showing the absorption bands of the chromophore (520 and 326 nm) compared to the spectrum of compound **3** in ethylene glycol (black line). The normalized two-photon absorption spectrum (red line + scatter) is reported on the same figure for comparison. (F) Normalized fluorescence emission spectra upon one photon excitation of free dye (compound **3**, black line) in methanol and **NP3** nanoparticles (red line) suspended in water. Upon excitation at 510 nm, the maximum emission values are 658 and 682 nm, respectively. The two-photon fluorescence spectrum obtained upon 1000 nm excitation of aqueous dispersion of **NP3** is indicated in dark yellow.

Fluorophore coupling to NPs (NP3)

One of the principal requirements for two-photon fluorescence imaging of biological media is that the dyes emit fluorescence in the red-near infrared (NIR) spectral range, where the auto-fluorescence from the medium is minimal and light is less scattered. The Lemke-type[25] fluorophore **3**, used in the present work was specifically designed for fluorescence imaging in bio-

logical media. As previously reported, this type of molecule was characterized by a strong dipolar donor–acceptor push–pull structure, which induces favorable optical spectroscopic properties suitable for imaging in the first biological transparency window (700–1000 nm).[23,26,27] Coupling of **3** with **NP2** was performed without use of copper catalyst, *via* thermally induced Huisgen-type 1,3-cycloaddition[28] to obtain **NP3**. Thermal activation of the reaction was preferred here to avoid use of toxic copper(II) ions for *in vivo* application. This coupling occurs between the azide functions on the surface of **NP2**, and the alkyne functions of fluorophore **3**, resulting in a strong bonding through imidazole cycle. In order to confirm the fluorophore grafting on **NP3**, infrared spectroscopy was used (Fig. S3A†). The vibration bands of PEG moieties (2869 cm^{-1} and 1100 cm^{-1}) and BP end-groups (1248 cm^{-1} around 1099 cm^{-1}, 946 cm^{-1} and 845 cm^{-1} for P=O, P–O and P–O(H) stretching vibrations respectively)[16,29] remain unchanged while the one corresponding to –N$_3$ groups (2100 cm^{-1}) disappears along with the reaction advancement (Fig. S3A† inset), clearly evidencing the coupling with **3**.

Interestingly, in spite of water-insolubility of **3**, the purified nanoparticles **NP3** were perfectly dispersible in aqueous medium, resulting in a pale pink-color homogeneous colloidal suspension. DLS measurements of **NP3** showed a slight increase in the average hydrodynamic size (28 ± 8 nm) due to the presence of the polymeric coating. The measured zeta-potential value is −42 ± 6 mV. The high stability of the particles is thus explained by both electrostatic and steric interactions. The authors attribute zeta potential decrease from −28 ± 3 mV (**NP2**) to −42 ± 6 mV (**NP3**) to the modification of coordination modes of bisphosphonate groups on the particle surface. The coordination of multidentate bisphosphonate moiety, which is the anchoring function of the ligands seem to be reorganized due to the heat-treatment during the coupling reaction. Increasing the proportion of not complexed P–O$^-$ bonds lead to the lower negative zeta potential. XPS analysis of the high-resolution spectrum centered on O 1s (Fig. S4C2†) supports this hypothesis. The measured binding energy band was decomposed to two contributions with peak maxima at 532.21 eV (61.11%) and 530.70 eV (38.89%), which were attributed to O–Gd and (H)O–P binding energies respectively. XPS elemental analysis (Table S1†) releal F/Gd ratios of 0.39 and 0.60 for **NP1** and **NP3** particles, respectively. The apparent Gd depletion is explained by partial shielding of surface gadolinium ions, due to the presence of the organic ligands (12.2 at% of carbon atoms on **NP3** compared to 0% on **NP1**) in the case of **NP3**. High-resolution XPS spectra (Fig. S4†) show that the binding energy of Gd 3d5/2 appears at 1187.8 eV for **NP1** and at 1188 eV for **NP3**. The peak Gd 4d5/2 appears at 142.7 eV for **NP1** and at 143.4 eV for **NP3**, which are attributed to GdF$_3$ compound.[30] Upon functionalization the peaks of Gd 4d are not significantly changed, suggesting, that the inorganic core retains its composition. The peak F 1s was detected at 684 eV for **NP3**, which also corresponds to the form GdF$_3$.[30]

NP2 was incubated with compound **3** in the usual conditions, without heating, in order to confirm unambiguously that compound **3** is covalently bonded and not adsorbed through weak interactions with PEG chains present on the surface. The resulting mixture was purified through centrifugation cycles and analyzed by UV-visible absorption spectroscopy (Fig. S3B†). The resulting absorption spectrum showed only the scattering profile of the particles and no absorption band associated to the fluorophore was observed. This is consistent with the fact that **3** does not react without heating and conversely the covalent bonding of the fluorophore to the particle surface was confirmed for **NP3**. Finally, TEM observations were performed on **NP3** to verify the stability of the GdF$_3$ core during the heating process, (Fig. 1C). TEM images showed similar morphology size and shape, as the initial particles.

Linear spectroscopy characterization of NP3

Before using **NP3** for *in vivo* experiments, the preservation of the optical properties of **3** when coupled to the nanoparticle was evidenced by absorption and emission spectroscopy. The UV-visible spectrum of **3** was recorded in three different solvents to evaluate the effect of environment polarity on spectral properties (Fig. S5†). In all three cases, a strong and structureless band appears between 400 and 650 nm accompanied by a smaller intensity band at shorter wavelengths (from 250 to 400 nm). Peak maxima are undergoing a slight shift due to solvatochromic effect, confirming that the fluorophore **3** is sensitive to its environment. The absorption spectrum of **NP3** (Fig. 1D) shows a band in the 450–600 nm range, above the continuous scattering background created by the particles. To determine the exact position of band maximum and be able to compare **NP3** with **3**, the absorption spectrum of **NP2** was subtracted from **NP3** spectrum (Fig. 1D). The resulting curve (green line) reveals the absorption profile observed for **3** in the **NP3** environment, with a peak maximum value at 520 nm slightly red-shifted. This demonstrates that after grafting on the particles, **3** is in a highly polar medium. Indeed, the subtracted spectrum (green line) and the absorption of **3** dissolved in EG are similar (Fig. 1E) in good agreement with the fact that on the surface of the particle, **3** is surrounded by the PEG chains.

Fluorescence emission and excitation spectra were recorded for fluorophore **3** in different solvents and in water for **NP3**. The spectroscopic results were summarized in Table 1. As it is shown in Fig. S6,† fluorescence emission of **3** undergoes a positive solvatochromism (red-shifted maxima) upon increasing solvent polarity; this is consistent with previous studies on similar dyes.[26] The maximum emission for **NP3** (Fig. 1F) is also in agreement with the solvent polarity dependence of the free dyes' series (positive solvatochromism). Upon excitation at 510 nm of **NP3** in water, the maximum emission detected is centered at 682 nm. It is very unlikely that the highly lipophilic fluorophore **3** is surrounded by water molecules in the **NP3** configuration. Instead, the polar PEG chains on the particle surface offer a more favorable environment, which is in accordance with the previous observations from absorption spectroscopy (Fig. 1E).

Table 1 Relevant spectroscopic properties of compound **3** in different solvents and **NP3** in water

	λ_{max} (nm)	$\varepsilon(\lambda_{max})$ (mM^{-1} cm^{-1})	λ_{em}^a (nm)	$\Delta\tilde{\nu}^a$ (cm^{-1})	RQY^a
3					
In DCM^b	505	32 800	634	4029	0.01
In ACN^b	500	29 200	653	4686	0.03
In MeOH^b	507	37 000	658	4527	0.12
NP3					
In H$_2$O	520	—	682	4568	0.03
Scattering corrected^c					0.13

^{a} λ_{ex} = 510 nm, RQY: relative quantum yield; reference Erythrosine B[31] in methanol (QY$_{ref}$ = 0.09). ^{b} DCM: dichloromethane; ACN: acetonitrile; MeOH: methanol. ^{c} The absorption spectrum is corrected for scattering and the corrected absorbance value is used to determine the RQY.

As mentioned before, absorbance of **NP3** is highly dominated by scattering. The absorbance value at the excitation wavelength (λ_{exc} = 510 nm), used for relative quantum yield determination, results in an apparent quantum yield of only 3%. However, by considering the subtracted spectrum, without scattering (Fig. 1D, green line), a more realistic value of absorbance is obtained with a calculated quantum yield of 13%. This value is in accordance with the results found for **3** in polar solvents such as methanol (Table 1), suggesting that the fluorescence of **3** is not altered upon the coupling to the particle.

Two-photon absorption (TPA) spectroscopic characterization of NP3

Two-photon spectroscopic properties of **NP3** were evaluated prior to *in vivo* two-photon microscopy imaging. Characterization of the two-photon absorption (TPA) cross sections of **NP3** at different wavelengths was performed by measuring the two-photon induced excitation spectrum[32,33]

and comparison to a known reference. The TPA spectrum of **NP3** was determined between 830 and 1000 nm, the tuning range of the excitation source being limited to the maximum of 1000 nm. Consequently, only the blue-side of the TPA spectrum is characterized. According to the absorption spectrum corrected for scattering, the concentration of fluorophore **3** in **NP3** suspension used to evaluate the TPA cross-section values (σ_{TPA}) is 16 μM. At 980 nm, the excitation wavelength of our two-photon microscopy experiments, the σ_{TPA} is approximately 30 GM. This value is significantly lower than fluorophores of similar structures in solution.[27] This discrepancy is explained by the important decrease of the excitation and emission intensity due to the high scattering induced by particles in our TPA characterization configuration (see Experimental details). For this reason, the normalized TPA spectrum of **NP3** is presented in Fig. 1E (red scatter + line) and not the absolute σ_{TPA} values. As previously observed for the chromophore **3**,[26] this spectrum overlaps with the blue part of the linear absorption of **NP3**.

The TPA-induced fluorescence spectrum of **NP3**, shown in Fig. 1F (yellow line), matches well with its one-photon excited counterpart (Fig. 1F, red line), showing that the fluorescence originates from the same excited state in both cases. This observation justifies the use of the fluorescence detection for the characterization of the TPA cross-section.

Magnetic resonance relaxivity measurements

T_1 and T_2 relaxation time values were determined at 7 T in saline and at room temperature from T_1 and T_2 maps (Fig. 2A). The r_1 and r_2 relaxivities of **NP3** were calculated, using the following formulas: $1/T_1 = r_1 \times C + 1/T_{1,0}$; $1/T_2 = r_2 \times C + 1/T_{2,0}$ (T_1 and T_2 in seconds; C = molar concentration in mmol L^{-1} and $T_{1,0}$ and $T_{2,0}$ are the relaxation times without contrast agent). A linear regression was made between the gadolinium concentration (mM) of **NP3** phantoms and the associated values $1/T_1$
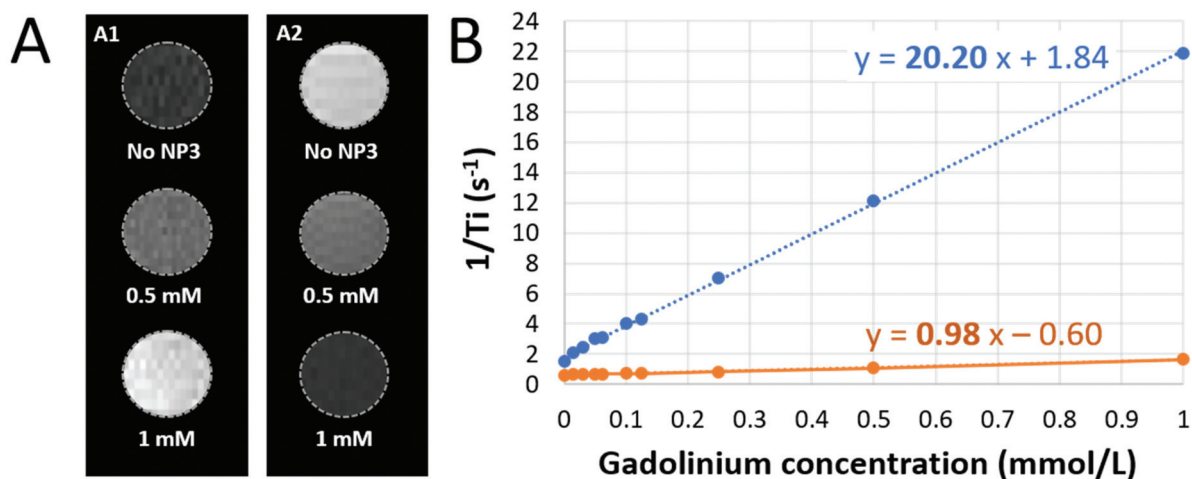

Fig. 2 (A) **NP3** relaxivities. On T_1-weighted images, MR signal increases with gadolinium concentration increase (A1) whereas on T_2-weighted images, MR signal drops with the increase of gadolinium concentration (A2). (B) Measurement of r_1 (orange) and r_2 (blue) relaxivities by linear regression connecting **NP3** phantoms gadolinium concentration to the value "$1/T_i$", where T_i means either T_1 or T_2.

or $1/T_2$. The slope of the line represents r_1 or r_2 (mM^{-1} s^{-1}), respectively (Fig. 2B).

The estimated r_1 and r_2 relaxivities of **NP3** are 0.98 mM^{-1} s^{-1} and 20 mM^{-1} s^{-1}, respectively, leading to a r_2/r_1 of 20.2. The r_2/r_1 value found here is close to the value observed for the ultrasmall superparamagnetic particles of iron oxide (USPIO), a well-known T_2/T_2^* MR contrast agent. Indeed, at the same magnetic field, the r_2/r_1 of the commercially available USPIO Ferumoxytol is 21.9.[34] Thus, **NP3** appears to possess promising T_2/T_2^* contrast properties at the concentrations that are expected *in vivo* and was further evaluated *in vivo* using T_2 and T_2^*-weighted MR sequences, in line with our previous observations.[16]

In vitro cytotoxicity assessment

Toxicity is a major concern regarding nanoparticles used in bio-imaging and especially when *in vivo* experiments are performed. In our specific case, prior to run *in vivo* imaging studies, the nanoparticle **NP3** cytotoxicity was evaluated on several human cell lines: THP-1 monocytes, HepG2 hepatocytes, A549 epithelial-like cells and HEK 293T kidneys cells. Two complementary assays, LDH and MTT, were used to investigate the potential impact of **NP3** on both mortality and metabolic activity of the cells incubated during 48 h and 72 h. The concentration of Gd in the culture medium ranges between 0 and 5 μM. All the LDH tests were compared to a positive control inducing 100% cell death. In all cases, the percentage of specific cytotoxicity is below 10% regardless of the cell lines, the **NP3** concentration or the incubation time (Fig. 3A). In the case of the MTT assay, the metabolic activity of non-exposed cells was taken as reference of the survival and/or the proliferation of the cells (100%); all cell lines show a metabolic activity which remains constant, between 86 and 127%, independently of **NP3** concentration (Fig. 3B).

NP3 is internalized by bone-marrow derived macrophages *in vitro* without overt toxic effects

Internalization of **NP3** particles by immune phagocytic cells was investigated *in vitro*. Bone marrow-derived macrophage (BMDM) primary cultures were incubated with **NP3** particles for 24 h (technical details are described in the ESI†). We first investigated the presence of the particle red fluorescent signal with confocal microscopy. The confocal images showed an important accumulation of nanoparticles inside the cells for 0.5 mM and 1.5 mM **NP3** conditions (Fig. 4A2 and A3), but not in the control condition (Fig. 4A1). **NP3** internalization measured by flow cytometry supported these observations
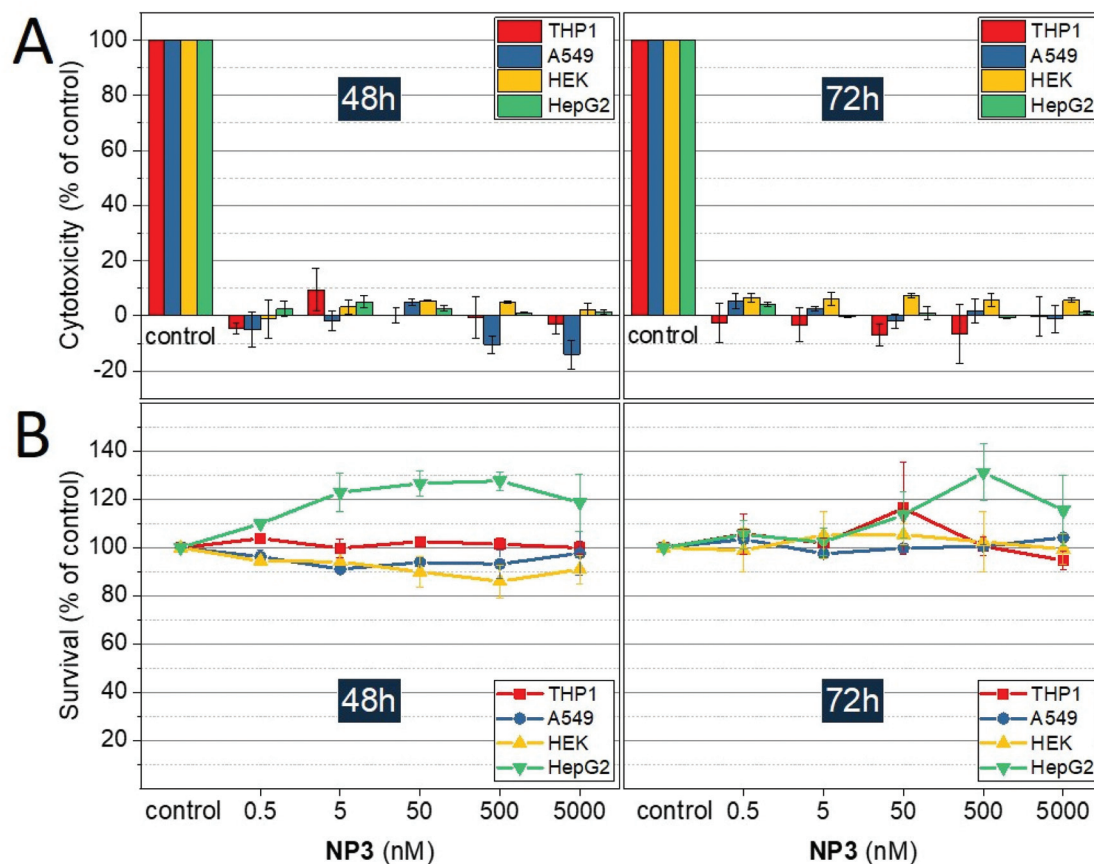

Fig. 3 Evaluation of **NP3** cytotoxicity. Cytotoxicity is measured in different human cultured cells: HepG2, HEK, A549 and THP1. Cells are incubated with 0–5 μM of **NP3** for 48 h and 72 h. (A) **NP3** impact on cell survival assessed by LDH assay. "Control" corresponds to the positive control with 100% cell death. Mean ± SD of duplicates. (B) **NP3** effect on cell viability assessed by MTT assay. Mean ± SD of duplicates.
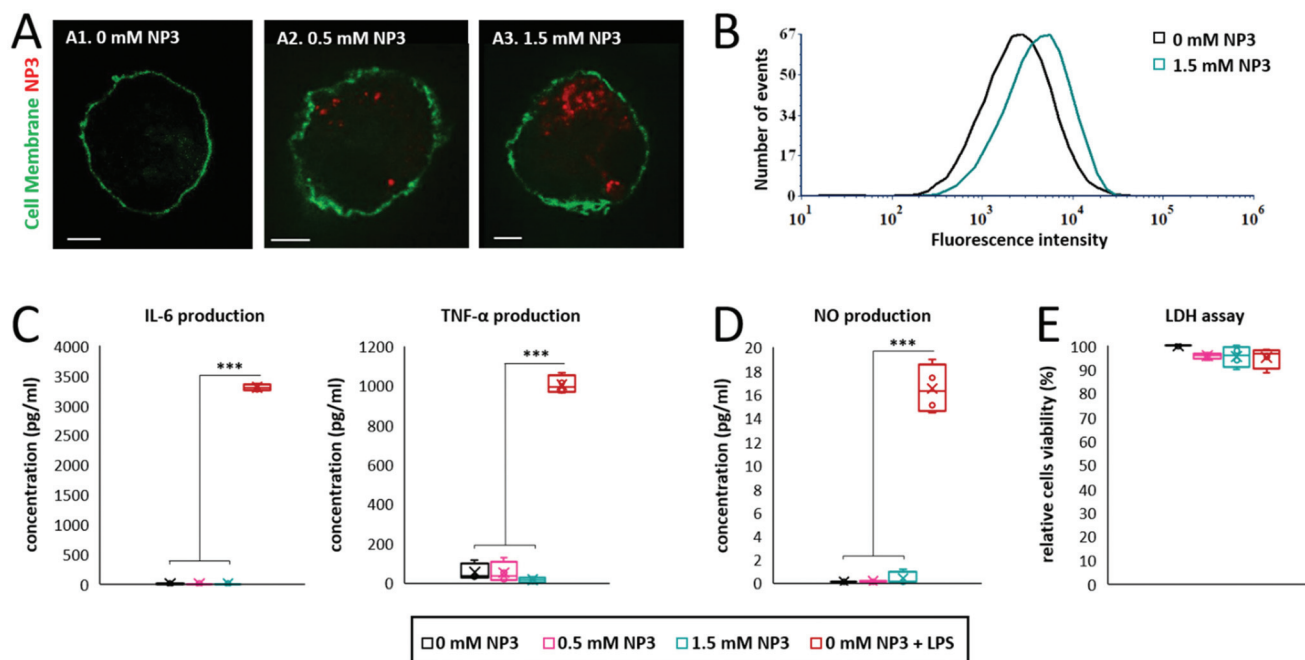
Fig. 4 NP3 is internalized by BMDM and is not associated with cytotoxicity. (A) Confocal images of primary BMDM incubated with NP3 (A2, 0.5 mmol L^{-1}; A3, 1.5 mmol L^{-1}) or without NP3 (A1). BMDM cell membranes labelled with FITC conjugated cholera toxin are detected in green and NP3 in red (scale bars: 5 μm). (B) Flow cytometer analysis shows the proportion of BMDM cells positives for NP3 for BMDM incubated with 1.5 mmol L^{-1} NP3. BMDM cells not incubated with NP3 (0 mM NP3) were used as control of NP3 negative cells. (C) Quantification of interleukin-6 (IL-6) and tumor-necrosis factor alpha (TNF-α) production by BMDM exposed to NP3. (D) Quantification of nitric oxide production by macrophages exposed to NP3. (E) Assessment of cell viability after exposition to NP3. For C to E experiments, cells exposed to LPS but not to NP3 (condition "0 mM NP3 + LPS") were used as a positive control of inflammatory environment. Significant differences calculated with a one-way ANOVA for $n = 4$ independent experiments are indicated by *** for $p < 0.005$. w/o: without.

(Fig. 4B). Pro-inflammatory cytokines, such as interleukine-6 (IL-6) and tumor-necrosis factor-α (TNF-α) play a key role in neuroinflammation. Therefore, we assessed their production by BMDM cultures exposed to NP3 particles and compared it to IL-6 and TNF-α production by non-exposed control BMDMs (Fig. 4C). No significant difference has been observed for IL-6 and TNF-α production by NP3-treated and non-exposed cells. By contrast, BMDM exposed to lipopolysaccharide or LPS (Fig. 4C, red signal), used as a positive control for pro-inflammatory cytokine production, was associated with significantly higher concentrations of IL-6 and TNF-α. This observation suggests that NP3 particles did not induce inflammation. In addition, BMDM exposure to NP3 was not associated with increase of nitric oxide (NO) concentration (Fig. 4D), thus suggesting that NP3 did not induce oxidative stress either. Finally, cell viability was not affected by NP3 exposure (Fig. 4E).

Altogether, these results (Fig. 3 and 4) demonstrate the lack of toxic effects of NP3 on the fate of the cells, highlighting the high level of safety of these nanoprobes and confirming their potential to be used further for *in vivo* imaging of phagocytic cells.

Biodistribution and pharmacokinetic profile of NP3

Biodistribution and pharmacokinetic of NP3 particles were evaluated *in vivo* in healthy mice by imaging the abdominal area with dynamic MRI. There was only a slight enhancement in the kidneys. In contrast, there was a strong accumulation of NP3 in the spleen during the first hours after injection (Fig. 5A), and, to a lesser extent in the liver, suggesting that NP3 is taken up by phagocytic cells from the reticuloendothelial system. From the vessel data (Fig. 5B), we concluded that NP3 has a long vascular remanence (>6 h). Therefore, the post-NP3 MRI scan was scheduled 48 h post-injection to allow sufficient time for nanoparticles elimination from the vascular compartment at the time of scanning. The long vascular remanence is an advantage for accumulation of the contrast agent in the brain in presence of a dysfunctional brain blood barrier as encountered in ischemic stroke.

Multimodal imaging in a mouse model of ischemic stroke

Nanoparticle NP3 was applied as a contrast agent for *in vivo* brain imaging in CX3CR1-GFP/+ mice with green-fluorescent microglia/macrophages subjected to permanent middle cerebral artery (pMCAo). The suspension of NP3 was intravenously injected into the mouse tail vein at the dose of 2 mmol Gd per kg and the animal's brain was imaged with MRI and intravital two-photon excitation microscopy (TPEM), before and after the injection of the contrast agent.

Fig. 6 shows T_2-weighted MR images (T_2-WI) pre- and post-NP3 injection. The ischemic lesion appeared as a hyperintense
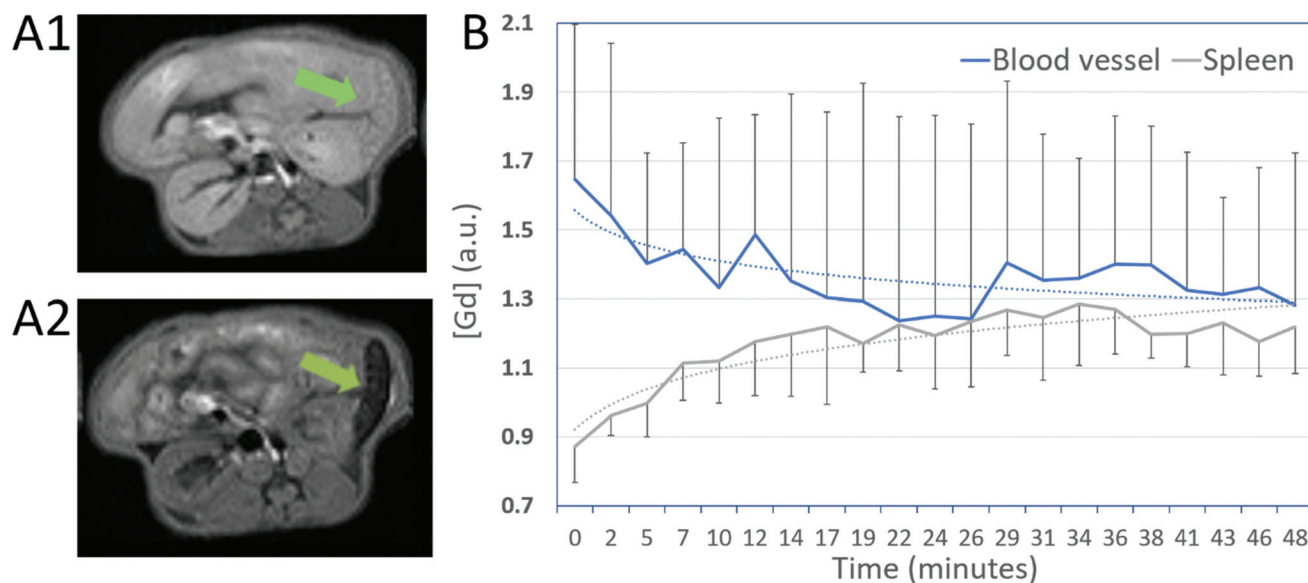
Fig. 5 Biodistribution and pharmacokinetic. (A) **NP3** biodistribution and pharmacokinetic were assessed with a dynamic sequence in the abdomen. A1: before gadolinium injection and A2: after gadolinium injection, at the end of the dynamic sequence. Green arrow points to the spleen. (B) Graph represents the evolution of MR signal intensities due to gadolinium associated with **NP3** in the spleen and the blood compartment across time after the first pass. Mean $\pm$ SD ($n = 4$).
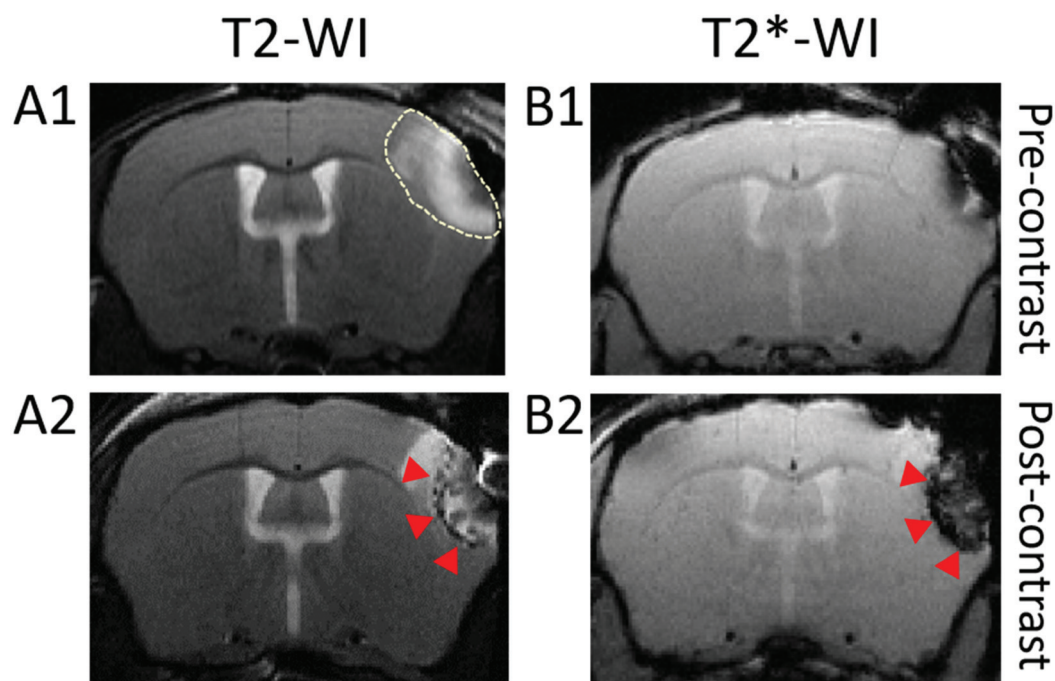

Fig. 6 *In vivo* **NP3**-enhanced MRI. (A1 and B1) Pre- and (A2 and B2) post-**NP3** injection T_2- and T_2*-weighted images (WI) of a pMCAo mouse brain. The ischemic lesion is seen as a hyperintense signal in T_2-WI (dotted line, A1). Accumulation of the nanoparticles in the ischemic area is characterized by the presence of hypointense signal voids in the lesion on post-**NP3** T_2-WI (A2, red arrowheads) and T_2*-WI (B2, red arrowheads).

signal (dotted line) in pre-**NP3** T_2-WI (Fig. 6A1). On the T_2-WI post-contrast images (Fig. 6A2), signal voids due to the nanoprobe are clearly distinguished inside the lesional area (red arrowheads, ischemic core). Signal voids were also detected

within the ischemic core on T_2*-WI (red arrowheads, Fig. 6B2). This confirms the potential of **NP3** as a T_2 and T_2* contrast agent and shows the ability of the probe to accumulate inside the ischemic lesion. The main advantages of this approach

compared to nuclear imaging ones is three-fold: first, it allows the imaging at the acute stage of ischemic stroke (3 days post-onset) which is currently not achievable with PET coupled to the administration of TSPO tracers; second, its provides a better spatial resolution in the mouse brain together with accurate morphological lesion depiction; and third, it opens the way to longitudinal tracking of labelled macrophages without the need for additional injection.

TPEM imaging offers the possibility to observe the cortical area at the subcellular scale, completing whole-brain MR imaging.

In a first series of experiments, CX3CR1-GFP/+ cells were observed by intravital TPEM in the parenchyma of a control mouse, as well as blood vessels that appear empty on the

image before injection of **NP3** (Fig. 7A). Immediately after injection, an intense signal was detected in the blood vessels, indicating the presence of nanoparticles in the blood flow (red signal in Fig. 7B). Going further, CX3CR1-GFP/+ mice subjected to pMCAo were imaged with TPEM. When looking at the core of the ischemic lesion, **NP3** nanoparticles were observed in blood vessels (Fig. 7C) and an important number of CX3CR1-GFP/+ cells colocalized with the **NP3** fluorescent signal (yellow signal in Fig. 7D), suggesting that the nanoparticles are effectively internalized by activated microglial cells and macrophages. Thus, the **NP3**-labeled cells become visible and directly observable in TPEM. Of note, the nanoparticles were still detected with TPEM in the blood vessels 24 h post-**NP3** administration (Fig. S7†), further confirming
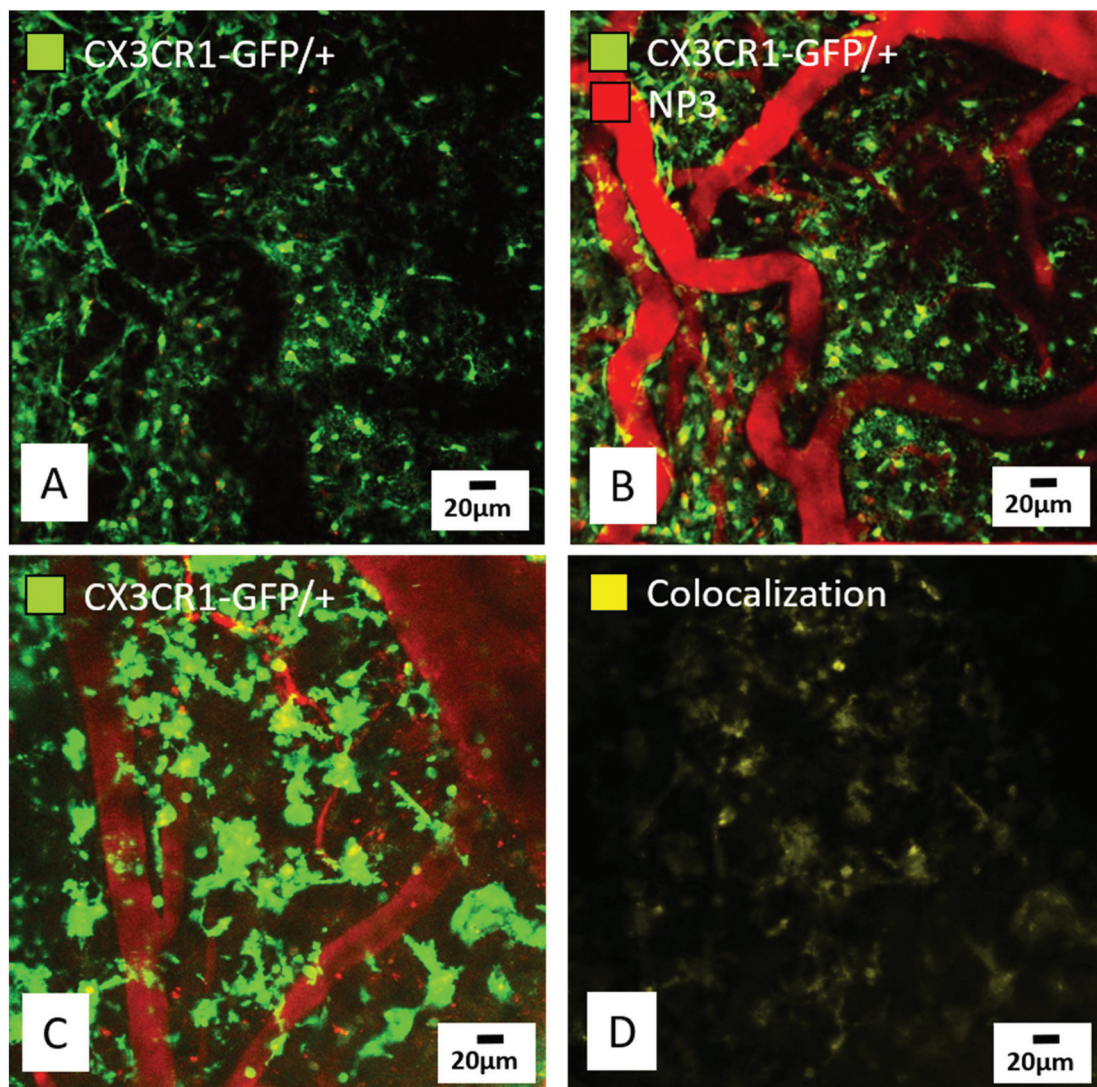

Fig. 7 Observation of the **NP3** *in vivo* in different brain compartments using two-photon microscopy. (A and B) Representative images of the parenchyma and blood vessels pre- (A) and post-**NP3** injection (B) in a control mouse showing resting CX3CR1-GFP/+ cells (in green) with ramified morphology. The nanoparticles (in red, B) are observed in the blood vessels immediately after injection, but not in the brain parenchyma. (C) In a pMCAo mouse, at the core of the lesion, the nanoparticles are present in vessels and inside activated CX3CR1-GFP/+ cells. (D) Nanoparticles are internalized by CX3CR1-GFP/+ cells: yellow signal corresponds to the colocalization of CX3CR1-GFP/+ cells (green signal in C) and the nanoparticles (red signal in C).
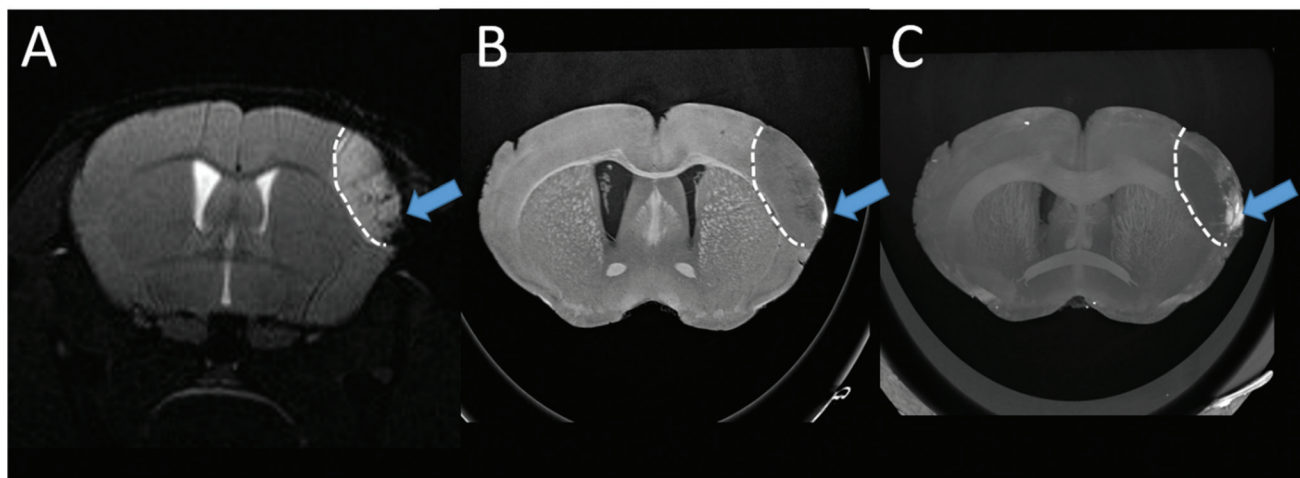
Fig. 8 *In vivo* T_2-WI image (A) and *ex vivo* phase–contrast computed tomography images (B and C) for the same pMCAo mouse injected with **NP3**. Hypointense signals on *in vivo* T_2-WI (A, blue arrow) colocalizes with hyperdense signals observed on native image (B, blue arrow) and maximum intensity projection (MIP) obtained with phase contrast image (C, blue arrow) and corresponding to the presence of Gd in the lesion. Dotted white line delineate the ischemic lesion.

the long (>6 h) vascular remanence of **NP3** observed during the pharmacokinetic study.

In order to ascertain that **NP3** nanoparticle was stable *in vivo* and hence that the GdF$_3$ core was also found in the brain parenchyma (*i.e.* in the regions where we detected the red fluorescence of the grafted fluorophore), mice brains have been perfused to wash out the vascular sector, sampled and scanned with synchrotron radiation phase contrast imaging. This innovative technique is based on the imaging of X-ray refraction rather than absorption thus resulting in enhanced contrast of soft tissues while allowing the accurate detection of metal-based contrast agents in the whole brain at microscale-resolution.[15,35] The gadolinium of **NP3** nanoparticles are clearly seen inside the ischemic lesion as a hyperintense signal that co-localizes with MR signal voids (Fig. 8). In summary, **NP3**-labeled macrophages could be imaged with three complementary imaging modalities, at different scales: MRI (~100 μm), intravital microscopy (~10 μm) and synchrotron X-rays (~1 μm). Such multi-scale approach is crucial in order to decipher the macrophage response at the early stage of ischemic stroke.

Conclusions

A hybrid GdF$_3$ contrast agent **NP3** was developed and fully characterized for multimodal and multiscale imaging of phagocytic cells. The inorganic core composed of highly crystalline GdF$_3$, one of the most stable compounds of gadolinium, shows good properties for MR and X-ray imaging. The PEG layer strongly anchored to the particle through bisphosphonate moieties confers biostability to the nanoparticle. **NP3** has a relatively small hydrodynamic diameter, a long vascular remanence and a negative zeta potential, all properties which

are known to be associated with greater uptake by macrophages.[36,37] *In vitro* cytotoxicity assessments performed on four human cell lines and on bone marrow-derived macrophages revealed no toxic effects. A two-photon active red-fluorophore coupled to the PEG-functionalized nanoparticle provided additive efficient contrast-enhancement properties for *in vivo* two-photon fluorescence imaging with resolution at the molecular scale.

The proof-of-concept that **NP3** nanoparticle may be used as a contrast agent targeting phagocytic cells was provided *in vitro* using bone-marrow derived macrophages and *in vivo* in an animal model of ischemic stroke using transgenic CX3XR1-GFP/+ mice. *In vivo* mouse brain MR imaging revealed the accumulation of the particles in the ischemic lesion, which is further confirmed by post-mortem *ex vivo* synchrotron radiation phase contrast imaging. The presence of the particles inside phagocytic cells was evidenced *in vivo* by TPEM observations, which indicates the internalization of the contrast agent by cells involved in neuroinflammation. Full validation of the imaging approach in a preclinical study of mice with ischemic stroke is ongoing.[38] The next step will be to take advantage of gadolinium for specific imaging with spectral photon counting CT in order to eliminate the need for pre-contrast scanning. Both these imaging approaches are technically challenging due to their lower sensitivity, therefore necessitating further dedicated developments. Nevertheless, our results clearly demonstrate the preclinical potential of hybrid GdF$_3$ nanoparticles as a promising tool for imaging phagocytic cells in neuroinflammatory diseases with multiscale resolution from macroscopic down to cellular level. Such preclinical imaging tool is crucial to select the immunomodulatory treatments that reach their target and may thus be translated into the clinics.

Author contributions

SK, FL, FC and SP designed, synthetized and characterized the nanoparticle. YB and CA designed the fluorophore. SK, YB, GM, AB and MLi performed the optical characterizations. MM and MLe designed the PEG ligands. AD, MMR and PNM assessed nanotoxicity. IH and OP realized the *in vivo* two-photon imaging and interpreted the data. VH and MW performed the MR imaging experiments and interpreted the data. VH and IH performed the surgeries. SK, VH, IH, FL, SP, MW and OP wrote the article. All authors approved the final version of the manuscript.

Conflicts of interest

There are no conflicts of interest to declare.

Acknowledgements

References

1 V. L. Feiding, B. Norrving and G. A. Mensah, *Circ. Res.*, 2017, **120**, 439–448.

2 U. Dirnagl, C. Iadecola and M. A. Moskowitz, *Trends Neurosci.*, 1999, **22**, 391–397.

3 Q. Wang, X. N. Tang and M. A. Yenari, *J. Neuroimmunol.*, 2007, **184**, 53–68.

4 B. Zinnhardt, M. Wiesmann, L. Honold, C. Barca, M. Schäfers, A. J. Kiliaan and A. H. Jacobs, *Theranostics*, 2018, **8**, 2603–2620.

5 C. Corot, K. G. Petry, R. Trivedi, A. Saleh, C. Jonkmanns, J.-F. Le Bas, E. Blezer, M. Rausch, B. Brochet, P. Foster-Gareau, D. Balériaux, S. Gaillard and V. Dousset, *Invest. Radiol.*, 2004, **39**, 619–625.

6 P. Chhour, P. C. Naha, S. M. O'Neill, H. I. Litt, M. P. Reilly, V. A. Ferrari and D. P. Cormode, *Biomaterials*, 2016, **87**, 93–103.

7 M. N. Bouchlaka, K. D. Ludwig, J. W. Gordon, M. P. Kutz, B. P. Bednarz, S. B. Fain and C. M. Capitini, *OncoImmunology*, 2016, **5**, e1143996.

8 S. Si-Mohamed, D. Bar-Ness, M. Sigovan, V. Tatard-Leitman, D. P. Cormode, P. C. Naha, P. Coulon, L. Rascle, E. Roessl, M. Rokni, A. Altman, Y. Yagil, L. Boussel and P. Douek, *Eur. Radiol. Exp.*, 2018, **2**, 34.

9 M. L. Cotrina, N. Lou, J. Tome-Garcia, J. Goldman and M. Nedergaard, *Neuroscience*, 2017, **343**, 483–494.

10 C. O. Schirra, B. Brendel, M. A. Anastasio and E. Roessl, *Contrast Media Mol. Imaging*, 2014, **9**, 62–70.

11 M. P. Menon and J. James, *J. Chem. Soc., Faraday Trans.*, 1989, **85**, 2683.

12 N. Halttunen, F. Lerouge, F. Chaput, M. Vandamme, S. Karpati, S. Si-Mohamed, M. Sigovan, L. Boussel, E. Chereul, P. Douek and S. Parola, *Sci. Rep.*, 2019, **9**, 12090.

13 S. de Reguardati, J. Pahapill, A. Mikhailov, Y. Stepanenko and A. Rebane, *Opt. Express*, 2016, **24**, 9053–9066.

14 H. Karatas, S. E. Erdener, Y. Gursoy-Ozdemir, G. Gurer, F. Soylemezoglu, A. K. Dunn and T. Dalkara, *J. Cereb. Blood Flow Metab.*, 2011, **31**, 1452–1460.

15 M. Marinescu, M. Langer, A. Durand, C. Olivier, A. Chabrol, H. Rositi, F. Chauveau, T. H. Cho, N. Nighoghossian, Y. Berthezène, F. Peyrin and M. Wiart, *Mol. Imaging Biol.*, 2013, **15**, 552–559.

16 F. Mpambani, A. K. O. Åslund, F. Lerouge, S. Nyström, N. Reitan, E. M. Huuse, M. Widerøe, F. Chaput, C. Monnereau, C. Andraud, M. Lecouvey, S. Handrick, S. Prokop, F. L. Heppner, P. Nilsson, P. Hammarström, M. Lindgren and S. Parola, *ACS Appl. Bio Mater.*, 2018, **1**, 462–472.

17 F. Chaput, F. Lerouge, S. Tusseau-Nenez, P.-E. Coulon, C. Dujardin, S. Denis-Quanquin, F. Mpambani and S. Parola, *Langmuir*, 2011, **27**, 5555–5561.

18 E. F. Chaput, C. Desroches and S. Parola, Method for Preparing Rare Earth Fluoride Nanoparticles; FR0954263, US 20120164049 A1, EP2445838A1, WO2010149918A1, EP2445838 (A1), 2009.

19 E. Ringe, R. P. Van Duyne and L. D. Marks, *Nano Lett.*, 2011, **11**, 3399–3403.

20 S. Kachbi-Khelfallah, M. Monteil, M. Cortes-Clerget, E. Migianu-Griffoni, J.-L. Pirat, O. Gager, J. Deschamp and M. Lecouvey, *Beilstein J. Org. Chem.*, 2016, **12**, 1366–1371.

21 Z.-Y. Yang, S.-L. Luo, H. Li, S.-W. Dong, J. He, H. Jiang, R. Li and X.-C. Yang, *RSC Adv.*, 2014, **4**, 59965–59969.

22 L. Sandiford, A. Phinikaridou, A. Protti, L. K. Meszaros, X. Cui, Y. Yan, G. Frodsham, P. A. Williamson, N. Gaddum, R. M. Botnar, P. J. Blower, M. A. Green and R. T. M. de Rosales, *ACS Nano*, 2013, **7**, 500–512.

23 S. Redon, J. Massin, S. Pouvreau, E. De Meulenaere, K. Clays, Y. Queneau, C. Andraud, A. Girard-Egrot, Y. Bretonnière and S. Chambert, *Bioconjugate Chem.*, 2014, **25**, 773–787.

24 Z. Varga, J. Mihály, Sz. Berényi and A. Bóta, *Eur. Polym. J.*, 2013, **49**, 2415–2421.

25 R. Lemke, *Synthesis*, 1974, 359–361.

26 J. Massin, W. Dayoub, J.-C. Mulatier, C. Aronica, Y. Bretonnière and C. Andraud, *Chem. Mater.*, 2011, **23**, 862–873.

27 J. Massin, A. Charaf-Eddin, F. Appaix, Y. Bretonnière, D. Jacquemin, B. van der Sanden, C. Monnereau and C. Andraud, *Chem. Sci.*, 2013, **4**, 2833.

28 R. Huisgen, *Angew. Chem., Int. Ed. Engl.*, 1963, **2**, 565–598.

29 F. Benyettou, J. Hardouin, M. Lecouvey, H. Jouni and L. Motte, *J. Bioanal. Biomed.*, 2012, **4**, 39–44.

30 *Handbook of X-ray photoelectron spectroscopy: a reference book of standard spectra for identification and interpretation of XPS data*, ed. J. F. Moulder and J. Chastain, Perkin-Elmer Corporation, Eden Prairie, Minn, Update., 1992.

31 N. Boens, W. Qin, N. Basarić, J. Hofkens, M. Ameloot, J. Pouget, J.-P. Lefèvre, B. Valeur, E. Gratton, M. vandeVen, N. D. Silva, Y. Engelborghs, K. Willaert, A. Sillen, G. Rumbles, D. Phillips, A. J. W. G. Visser, A. van Hoek, J. R. Lakowicz, H. Malak, I. Gryczynski, A. G. Szabo, D. T. Krajcarski, N. Tamai and A. Miura, *Anal. Chem.*, 2007, **79**, 2137–2149.

32 C. Xu and W. W. Webb, *J. Opt. Soc. Am. B*, 1996, **13**, 481–491.

33 N. S. Makarov, J. Campo, J. M. Hales and J. W. Perry, *Opt. Mater. Express*, 2011, **1**, 551–563.

34 S. Liu, J.-C. Brisset, J. Hu, E. M. Haacke and Y. Ge, *J. Magn. Reson. Imaging*, 2018, **47**, 621–633.

35 J. Albers, S. Pacilé, M. A. Markus, M. Wiart, G. Vande Velde, G. Tromba and C. Dullin, *Mol. Imaging Biol.*, 2018, **20**, 732–741.

36 C. Corot, P. Robert, J.-M. Idée and M. Port, *Adv. Drug Delivery Rev.*, 2006, **58**, 1471–1504.

37 E. Fröhlich, *Int. J. Nanomed.*, 2012, **7**, 5577–5591.

38 V. Hubert, I. Hristovska, S. Karpati, S. Benkeder, C. Dumot, C. Amaz, N. Chounlamountri, C. Watrin, J.-C. Comte, F. Chauveau, E. Brun, F. Lerouge, S. Parola, O. Pascual and M. Wiart, *Multimodal imaging with NanoGd reveals spatio-temporal features of neuroinflammation after experimental stroke*, 2021, submitted.